# Silver-Copper Oxide Heteronanostructures for the Plasmonic-Enhanced Photocatalytic Oxidation of N-Hexane in the Visible-NIR Range

Hugo Suarez [1], Adrian Ramirez [1,2], Carlos J. Bueno-Alejo [1,3] and Jose L. Hueso [1,3,4,*]

[1] Institute of Nanoscience of Aragon (INA) and Department of Chemical and Environmental Engineering, C/Poeta Mariano Esquillor, s/n; Campus Rio Ebro, Edificio I+D, 50018 Zaragoza, Spain; hasuarezo2@gmail.com (H.S.); adrian.galilea@kaust.edu.sa (A.R.); carlosj_bueno@yahoo.es (C.J.B.-A.)

[2] KAUST Catalysis Center (KCC), King Abdullah University of Science and Technology (KAUST), 23955 Thuwal, Saudi Arabia

[3] Networking Research Center on Bioengineering, Biomaterials and Nanomedicine (CIBER-BBN), 28029 Madrid, Spain

[4] Instituto de Ciencia de Materiales de Aragon (ICMA), Consejo Superior de Investigaciones Cientificas (CSIC-University of Zaragoza), 50018 Zaragoza, Spain

* Correspondence: jlhueso@unizar.es

check for updates

**Abstract:** Volatile organic compounds (VOCs) are recognized as hazardous contributors to air pollution, precursors of multiple secondary byproducts, troposphere aerosols, and recognized contributors to respiratory and cancer-related issues in highly populated areas. Moreover, VOCs present in indoor environments represent a challenging issue that need to be addressed due to its increasing presence in nowadays society. Catalytic oxidation by noble metals represents the most effective but costly solution. The use of photocatalytic oxidation has become one of the most explored alternatives given the green and sustainable advantages of using solar light or low-consumption light emitting devices. Herein, we have tried to address the shortcomings of the most studied photocatalytic systems based on titania ($TiO_2$) with limited response in the UV-range or alternatively the high recombination rates detected in other transition metal-based oxide systems. We have developed a silver-copper oxide heteronanostructure able to combine the plasmonic-enhanced properties of Ag nanostructures with the visible-light driven photoresponse of CuO nanoarchitectures. The entangled Ag-CuO heteronanostructure exhibits a broad absorption towards the visible-near infrared (NIR) range and achieves total photo-oxidation of n-hexane under irradiation with different light-emitting diodes (LEDs) specific wavelengths at temperatures below 180 °C and outperforming its thermal catalytic response or its silver-free CuO illuminated counterpart.

**Keywords:** plasmonic photocatalysis; silver-copper oxide; VOCs remediation; full-spectrum photoresponse

## 1. Introduction

Global warming, massive deforestation for urbanization and increasing contamination caused by mankind practices are contributing to the alarming rise of pollutant emission levels worldwide. Among these contaminants, the exposure to volatile organic compounds (hereafter VOCs) is recognized as a serious hazard to human health contributing to skin, respiratory, and cancer diseases [1–3]. Even if the exposure dose is very low, it has become an issue of increasing interest since many of the VOCs emitting sources are not only stemming from big factories or production plants. Indoor sources such as tobacco smoke, solvents, paints, furniture, computer, personal use products, etc. are continuously

contributing to the VOCs emissions in indoor habitats [1–5]. There are currently different exploring technologies devoted to VOCs remediation including the use of plasma discharges [6–9], microwaves combining absorption–desorption–combustion steps [10–12], photodegradation [2,5,13–20], and adsorption/catalytic oxidation [2,21–29]. Total oxidation of VOCs promoted by conventional catalysts represents one of the most appealing alternatives. Noble metals are able to completely oxidize VOCs into $CO_2$ and $H_2O$ at mild reaction temperatures [22,23,25,30–39]. Transition metal oxides and complex metal oxides (i.e., rare earth element-based perovskites) are also excellent VOCs oxidation candidates that operate at relatively mild temperatures without incurring in the burdening costs of noble metals [3,8,16,37–45]. Alternatively, the use of inexpensive arrays of photocatalysts based on titania ($TiO_2$) has become one of the most important research fields towards the sustainable remediation of VOCs [5,20,46–51]. The advantages of using solar light or low consume artificial lights to promote VOCs oxidation at room temperature is being actively pursued. Current limitations are found either in the weak response of the most active semiconductor photocatalysts (i.e., $TiO_2$, ZnO) beyond the UV range (that only represents 4%–5% of the full solar spectrum) or in the rapid electron-hole recombination rates detected in transition metal oxide semiconducting photocatalysts with expanded absorption capacities towards the visible-near infrared (NIR) ranges (i.e., $MO_x$, M = Cu, Fe, Mn, Co) [2,43,52–58].

To overcome these drawbacks, current research interests in VOCs remediation are focused on the development of hybrid nanomaterials combining metal oxides, metal transition oxides and/or noble metals with photocatalytic response expanded towards the visible-NIR ranges [16,21,59–69]. Metallic nanoparticles can play a determining role in expanding the absorption range of regular metal oxides such as titania ($TiO_2$) and/or reducing the electron-hole recombination rates of metal transition oxides (i.e., $MO_x$ (M = Fe, Mn, Co, Cu) [2,3,19,58,59,70–90]. Furthermore, metallic nanoparticles have become particularly relevant due to their plasmonic properties [2,76,81,86,91–96]. The localized surface plasmon resonance (LSPR) is a unique characteristic of these materials (normally Au, Ag, Pt, or other noble metals), which can extend the absorption of light towards the visible light spectrum [69,87–90]. Thus, LSPR greatly supports the utilization of the solar spectrum [69,81,92,97–104]. In addition, plasmonic nanoparticles may play active roles as sensitizers (via antenna effects) or accommodate charges from semiconductors upon forming effective Schottky metal-semiconductor junctions as in well-established noble metal-$TiO_2$ hybrid systems [69,92,97–100].

In the present work, we aimed at exploring the synthesis of a hybrid heterostructured catalyst combining the plasmonic properties of Ag and the p-type semiconductor capabilities of CuO [3,101–104]. Both materials are abundant, affordable, and exhibit a strong potential for full-range photocatalytic applications. Previous studies based on plasmonic silver nanostructures [76,92], $Cu_xO_y$ systems [105–107] or in the combination of silver-copper alloys [108–112], silver-copper oxide heterostructures [109,113–115] or even silver-copper oxide decorating $TiO_2$ [70,108] have already proved their potential not only in visible-NIR expanded photocatalysis [70,114,116], but also in solar harvesting, electrocatalysis, bacteria disinfection, field emission enhancement or the formation of novel superconducting structures [55,108,109,111,114–120]. Herein, we have demonstrated that these Ag-CuO heterostructures with an intertwined configuration maximize the plasmon-semiconductor interaction. As a result, a very active hybrid heterostructure with full-spectrum LED-driven photoresponse towards the total oxidation of n-hexane has been developed. Its photocatalytic response becomes especially photoactive upon irradiation with LED wavelengths of 460 nm. The heterostructure fully photooxidizes n-hexane at temperatures below 180 °C and outperforms its silver-free CuO counterpart thereby outlining the relevance of the silver nanostructures entangled with the CuO nanotubes in the Ag-CuO hybrid. To the best of our knowledge, this study presents the first example of full-spectrum photocatalytic assisted VOCs oxidation in a diluted gas phase with this kind of Ag-CuO configuration.

## 2. Materials and Methods

### 2.1. Synthesis of the Photocatalysts

The Ag-CuO heteronanostructures were synthesized following a protocol reported elsewhere [121]. $Cu(NO_3)_2 \cdot 3H_2O$ (3.2 mmol, Aldrich, Saint Louis, MO, USA, 99.9%) and $AgNO_3$ (3.1 mmol, Aldrich, Saint Louis, MO, USA, 99.9%) were dissolved in 3 mL of deionized water. The resulting silver-copper solution was added to an aqueous solution of NaOH 3 M (4 mL, Aldrich) with vigorous stirring for 6 h under an inert Ar atmosphere. The resulting black adduct that was vacuum filtered, washed with water, and dried at 100 °C for 2 h. The solid was calcined at 350 °C for 6 h. In order to obtain silver-free CuO nanostructures, an analogous synthesis protocol was followed but skipping the addition of the silver salt precursor. The synthesis of the photocatalysts has been performed at the platform of Production of Biomaterials and Nanoparticles of the NANBIOSIS ICTS, Spain, more specifically by the Nanoparticle Synthesis Unit of the CIBER in BioEngineering, Biomaterials & Nanomedicine (CIBER-BBN).

### 2.2. Characterization Techniques

Transmission electron microscopy (TEM) analysis was carried out using a T20–FEI microscope (Hillsboro, OR, USA). Aberration corrected scanning transmission electron microscopy (STEM) images were acquired using a high angle annular dark field detector in a FEI XFEG TITAN microscope (Hillsboro, OR, USA) at 300 kV equipped with a CETCOR Cs-probe corrector. High-resolution transmission electron microscopy (HR-TEM) images were acquired with the aid of a FEI TITAN[3] electron microscope operated at 200 kV. Elemental analysis was carried out with Energy Dispersive Spectroscopy (EDS) (EDAX, Mahwah, NJ, USA) detector using single point and scanning profiles. The samples were drop-casted onto Ni mesh grids. The $N_2$ adsorption/desorption analyses were performed with the aid of a Micromeritics ASAP2020 analyzer (Norcross, GA, USA). 80–100 mg of the catalyst was degassed at 90 °C for 12 h. The surface area was determined using the Brunauer–Emmett–Teller (BET) method rendering a value of 4.7 $m^2 \cdot g^{-1}$ for the Ag-CuO tubular heterostructures. Scanning electron microscopy (SEM) analysis was carried out with FEI-Inspect S50 equipment (Hillsboro, OR, USA). X-ray diffraction patterns were obtained in a PANalytical Empyrean equipment (Malvern, UK) in Bragg Brentano configuration using Cu-K radiation and equipped with a PIXcel1D detector. The absorption spectra were acquired with a JASCO V-670 UV-VIS-NIR spectrophotometer (Tokyo, Japan) and the aid of an integrated sphere accessory.

### 2.3. Photocatalytic Reaction Setup

The experimental setup designed to carry out the photocatalytic degradation of n-hexane has been previously described elsewhere [20,122]. Briefly, the reaction was conducted in a home-made system comprising a quartz cell ($50 \times 10 \times 5$ mm$^3$ (height × width × length). The cell was illuminated by two high power LEDs (LedEngin) cooled with the aid of custom-designed fans. Different LEDs wavelengths were individually tested. Each LED operated with different power: 405 nm (3.9 W), 460 nm (2.2 W), and 940 nm (3.2 W). Selected light irradiances ranged from 7 to 11,000 mW/cm$^2$ (based on LED specifications and experimental setup) and LED powers were programmed with the aid of an external power supply unit (ISO-TECH, IPS-405, 0–40 V). The temperature of the catalytic bed containing 300 mg of Ag-CuO during irradiation was monitored with the aid of a K-type thermocouple. The photocatalytic experiments were performed with a total flow of 50 mL·min$^{-1}$ of gas containing 200 ppm of n-hexane (space velocity = 10,000 h$^{-1}$). Conventional heating experiments were carried out with a home-built system consisting of an aluminium holder designed to heat the same reactor area as in the quartz reactor used for the photocatalytic test [20]. The inlet final concentration of n-hexane was achieved upon mixing with the proper flow rates, n-hexane in $N_2$, $O_2$, and synthetic air (all purchased from PRAXAIR España S.L.U., Madrid, Spain), in order to get the different total flow rates assessed. After an equilibration period of 30 min that served us to evaluate the adsorption of n-hexane in the dark, the LED lights were turned on for different time intervals and the gas effluent outlet analyzed by

gas chromatography (Agilent 3000 Micro GC, Santa Clara, CA, USA). An OV-1 and a PPQ column in line with a thermal conductivity detector (TCD) were employed to separate and detect the different gas compounds. The steady state final concentration achieved was always ≤10 ppm of n-hexane when maximum LED power was used. This steady state was always achieved within minutes regardless of the experimental settings. Under the conditions used, the n-hexane detection limit was 3 ppm and $CO_2$ was the only oxidation product detected. Maximum error in the mass balance closures for carbon and oxygen in this work was ±2%.

## 3. Results

### 3.1. Characterization of the Silver-Copper Oxide Plasmonic Photocatalyst

The morphological evaluation of the Ag-CuO heterostructures by SEM revealed the presence of tubular-shaped structures (Figure 1a) [121,123,124]. A more detailed analysis by HAADF-STEM in combination with EDX analysis confirmed the presence of both Ag and Cu species as segregated elements. Figure 1b–d reveal the corresponding analysis of the outer surfaces of the tubular structures. Small Ag nanoparticles are supported onto the Cu-based surface (Figure 1b,d). An extended EDX line profile analysis across two individual nanotubes further confirmed the alternating presence of either silver or copper elements (see Figure 1e–f).

It is also worth mentioning that Ag was identified with different morphologies, including small segregated nanoparticles, rod-shaped anisotropic structures (Figure 1g), and non-uniform aggregates dispersed along the tubular-shaped CuO matrixes (Figure 1i). HR-TEM analysis of the Cu-based regions confirmed the presence of a well-defined orientation corresponding to a CuO crystalline phase (Figure 1h). The FFT inset in Figure 1g corresponded to the orientation of the CuO fraction in the [0-1-1] direction. The (200), (11-1), and (-11-1) planes were identified and matched with a C2/c monoclinic system. EDX mapping of the intensities of Ag-L and Cu-L signals further assessed the entangled distribution of Cu (Figure 1j) and Ag phases (Figure 1k).

XRD analysis also corroborated the presence of both silver and copper oxide crystalline phases assigned to a cubic (Fm3m) and a monoclinic (C2/c) system, respectively (Figure 2a). The optical characterization of the Ag-CuO nanohybrids by UV-Vis-NIR spectroscopy revealed a broad absorption spectrum expanding towards the visible and near-infrared (NIR) range (Figure 2c). The silver-free CuO nanotubes synthesized as control (Figure 2b) exhibited similar optical absorption properties in the visible range, although it did not expand beyond the visible range and decayed in the NIR region (Figure 2c). The energy band gap for both the CuO and Ag-CuO nanostructures was determined from the optical absorption near the band edge using the classical Tauc approach and assuming an indirect band gap semiconductor system where $\alpha \cdot E_{photon} = K (E_{photon} - E_g)^{1/2}$ (being $E_{photon}$ and $E_g$ the discrete photon energy and the band gap energy, respectively). The estimated band gap energy was calculated at 1.33 eV for the CuO nanostructures and 0.71 eV for the Ag-CuO hybrids (Figure 2d). These values were lower than the band gap reported for bulk CuO structures (typically 1.4 eV) and confirmed the potential optical response of these structures in the visible-NIR range [53].
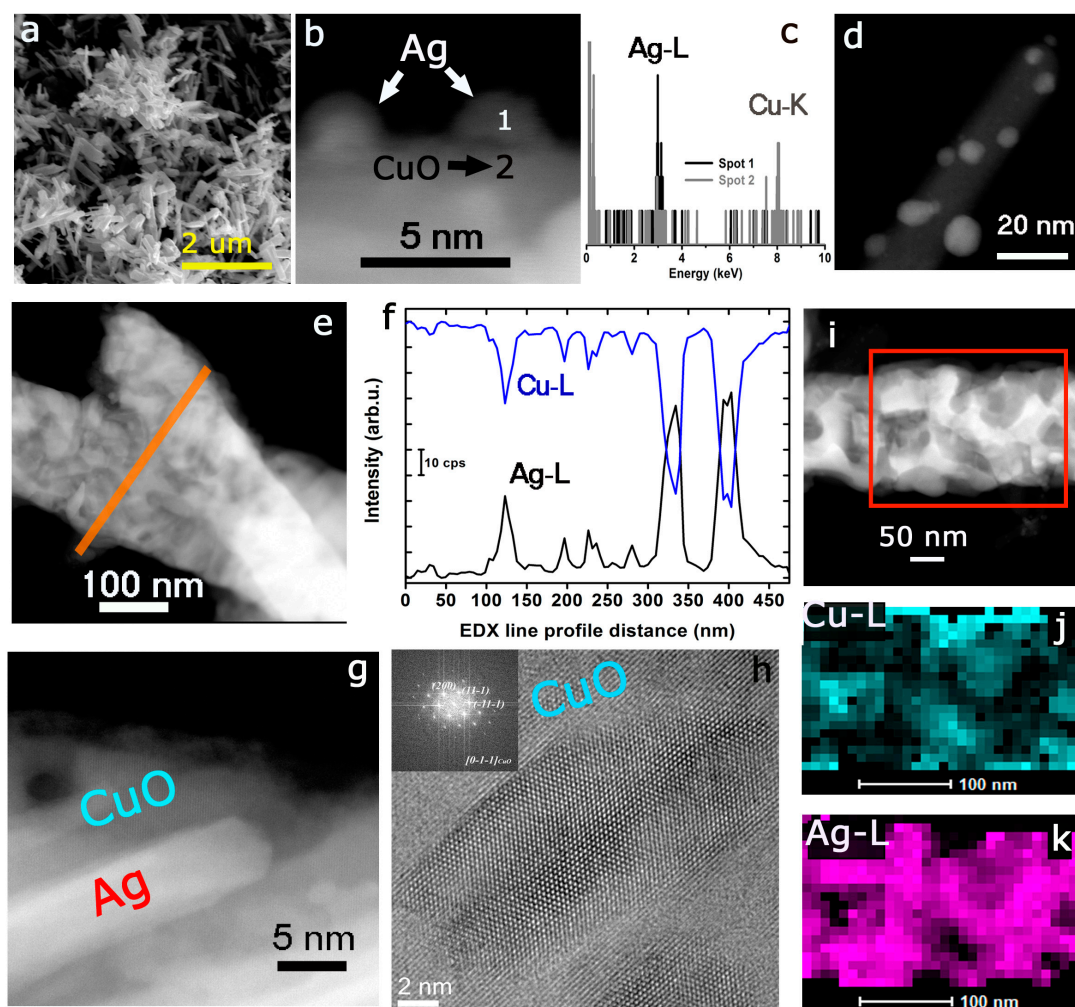
**Figure 1.** Morpho-chemical characterization of the silver-copper oxide photocatalyst: (**a**) SEM representative image accounting for the tubular shape of the Ag-CuO hybrids; (**b**) High Angle Annular Dark-Field (HAADF)-STEM image of small Ag nanoparticles (NPs) in the outer area of the nanotubes dispersed in a Cu-based matrix, the numbers refer to specific areas for EDX spectra acquisition; (**c**) EDX analysis of selected spots in (**b**) accounting for the specific present of Ag or Cu; (**d**) HAADF-STEM image of a CuO nanotube with Ag NPs decorating in the external region; (**e**) STEM image of individual nanotubes and EDX line profile analysis performed and plotted in (**f**); (**f**) evolution of Ag-L and Cu-L intensities across the EDX line profile analysis depicted in (**e**); (**g**) HAADF-STEM image accounting for the presence of anisotropic Ag shapes embedded within the Cu-based matrix; (**h**) HR-TEM image corresponding to the Cu-enriched region accounting for the presence of a monoclinic CuO phase (inset: Fast Fourier Transform (FFT) image with indexed CuO planes in the [0-1-1] direction); (**i**) HAADF-STEM image of a fraction of Ag-CuO nanotube containing bigger aggregates (the square accounts for the selected area for EDX mapping analysis); (**j**) EDX map accounting for the Cu-L edge (wt %) intensity in the selected area of (**i**); (**k**) EDX map accounting for the distribution of the Ag-L edge intensity (wt %) in the selected area of (**i**).
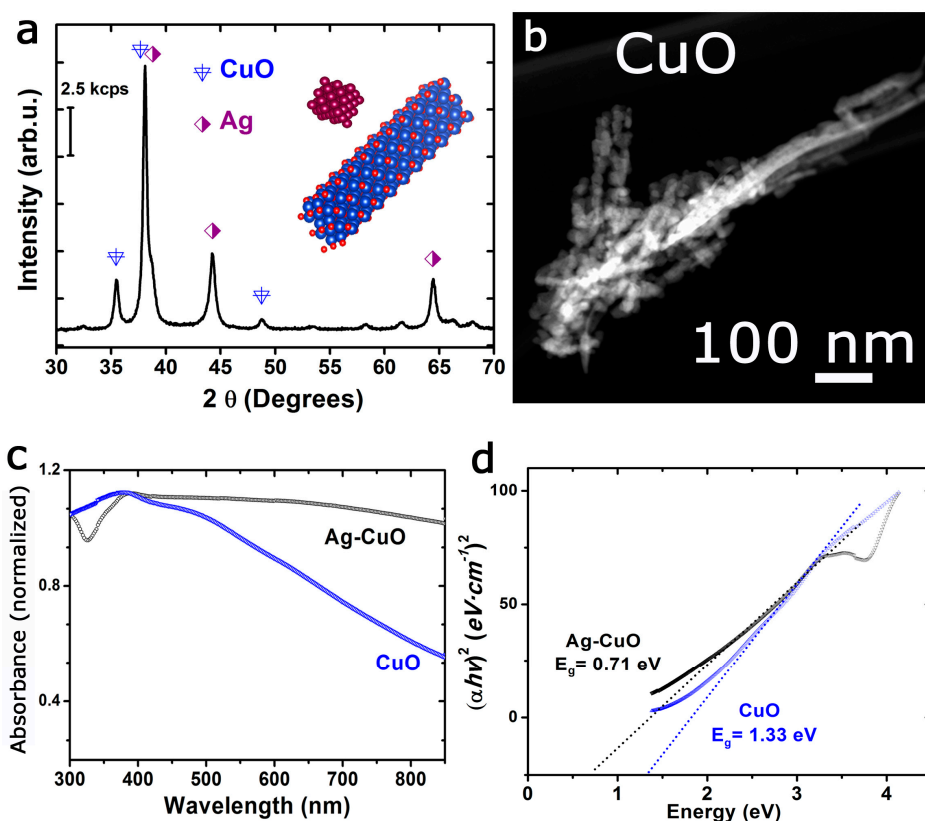
**Figure 2.** Additional characterization of the photocatalytic materials: (**a**) X-ray diffractogram of the Ag-CuO hybrid material accounting for the presence of both cubic and monoclinic crystallographic phases for silver and copper oxide, respectively; (**b**) HAADF-STEM representative image of the silver-free CuO nanostructures; (**c**) UV-Vis-Near Infrared absorption spectra of the Ag-CuO and CuO nanomaterials; (**d**) Tauc plots for the determination of the band gap energies for Ag-CuO and CuO structures assuming an indirect transition.

### 3.2. Photocatalytic Performance of the Ag-CuO Heterostructures for N-Hexane Total Oxidation

Figure 3 shows the photocatalytic response of the Ag-CuO hybrid towards the oxidation of n-hexane under illumination with a high irradiance LED emitting at 405 nm (see inset in Figure 3b). Total oxidation was achieved at temperatures below 180 °C. Remarkably, light-off oxidation curves started at temperatures below 50 °C and $T_{50}$ (Temperature of reaction required to reach 50% of conversion) remained below 100 °C. These results contrast with the photocatalytic behavior identified for the silver-free CuO counterpart under similar LED irradiation conditions. In this latter case, temperatures above 200 °C were necessary to reach match $T_{50}$ and a complete n-hexane oxidation was not achieved (maximum 90% conversion, see Figure 3a). Finally, it is worth mentioning that the thermal catalytic experiment (in the absence of LED irradiation) with the Ag-CuO catalyst yielded higher n-hexane conversion levels than the CuO catalyst but were less effective than the photocatalytic experimental conditions (Figure 3a).

Additional photocatalytic experiments were carried out with the Ag-CuO heterostructure under illumination with different LED wavelengths at 460 and 940 nm, respectively. The use of LEDs emitting in the visible and NIR ranges rendered equivalent n-hexane photo-oxidation levels and analogous overlapping light-off curves to the one displayed in Figure 3a (data not shown). The major differences were observed in terms of the LED power density required in each experiment to achieve those conversion levels. Figure 3b summarizes the LED power irradiance (expressed in W/cm²) required at 405, 460, and 940 nm, respectively. Upon comparison of the three LEDs, it became clear that the photocatalytic efficiency was higher at 460 nm. The irradiation under the LED emitting at 405 nm

required almost double irradiance to reach full photo-conversion of n-hexane. We observed a stable photo-response after multiple cumulative reaction runs performed under different LED wavelengths and no evidences of deactivation.
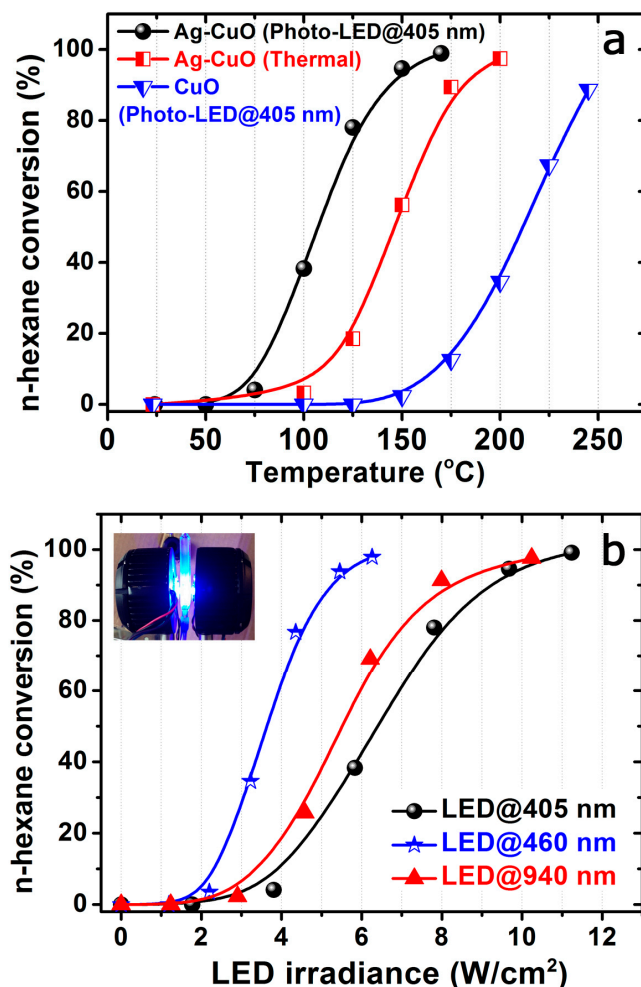


**Figure 3.** LED-driven photocatalytic oxidation of n-hexane: (**a**) n-hexane conversion curves obtained after photocatalytic activation of Ag-CuO (spherical symbols), CuO (triangle symbols) with a LED emitting at 405 nm, and alternatively after thermal heating of Ag-CuO with a conventional heating setup (square symbols); (**b**) n-hexane light-off curves under different irradiation wavelengths as a function of the irradiance (in W/cm$^2$) specifically required for each LED; (inset: Digital image of the 405 nm LEDs simultaneously irradiating the quartz cuvette reactor).

## 4. Discussion

The positive photocatalytic response towards n-hexane oxidation of the present Ag-CuO hybrid structures can be justified in terms of the synergetic combination of plasmonic silver and the visible-light response of the p-type semiconductor CuO. In contrast to previous Ag-Cu systems [55,108,109,111,114,117,119], our synthesis methodology enables the generation of a well entangled hybrid system where Ag domains of different sizes and morphologies are perfectly encapsulated within CuO nanotubes (Figures 1 and 2). The most plausible mechanism for the formation of this hybrid is the thermal decomposition of an unstable silver-copper mixed oxide $Ag_xCu_yO_z$ that evolves into the corresponding silver and copper oxides counterparts [125–127]. The thermal treatment at high temperature during the preparation also favored the subsequent thermal decomposition of $Ag_2O$ into metallic Ag and oxygen at temperatures in the range of 195–205 °C and enabling partial mobility of silver throughout the CuO tubular scaffold (Figure 1) [76,128].

To justify the full-range response under different LED wavelengths (Figure 3b), a combination of different photo-excitation and charge-transfer mechanisms can be taking place [68,69,81,99,129,130]. The different photocatalytic response observed after comparison between Ag-CuO and CuO irradiated with the 405 nm LED (Figure 3a) clearly demonstrates the positive influence of the silver entangled nanostructures. Given the heterogeneous disposition of silver entities, different photo-activation pathways can be simultaneously occurring in our catalysts. First of all, a fraction of smaller silver domains (Figure 1b–d) with the proper energy levels can be acting as sinks or trap centers for the electrons photogenerated by the CuO semiconductor fraction (Figure 4a). As a result, the expected high electron-hole recombination rates of CuO can be inhibited and/or partially delayed. Therefore, the unpaired holes remain available in the valence band of CuO to readily oxidize n-hexane molecules (Figure 4a). Likewise, electrons in the Ag surface can participate in the formation of reactive superoxide anions or relax via thermal energy dissipation [95,131]. The superoxide anions may subsequently react after their photo-induced dissociation (Figure 4a) and contribute to the oxidation of the n-hexane molecules [5,68,69,76,81,105,130,132].
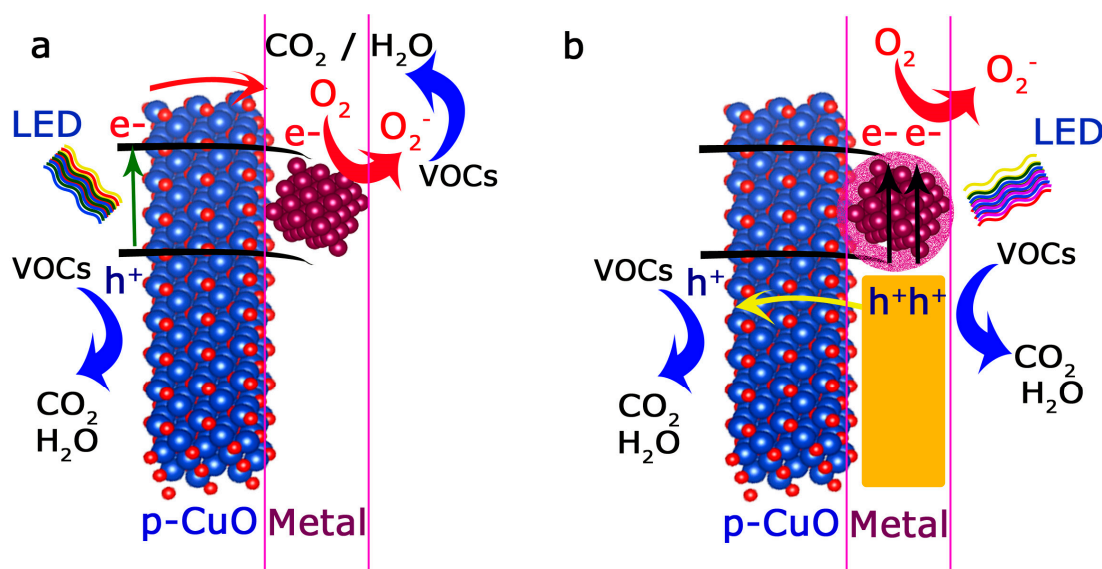


**Figure 4.** Schematic diagram illustrating the most plausible charge-transfer and photocatalytic mechanisms in the metal/p-type semiconductor Ag-CuO hybrids: (**a**) If the LED excitation wavelength is larger than the energy band gap of CuO, electrons from the valence band can be excited to the conduction of CuO and subsequently transferred and trapped by Ag energy levels; (**b**) Ag plasmon-induced charge transfer by hot holes injection into the p-type CuO energy levels.

Another fraction of silver structures with different sizes and anisotropic shapes (i.e., rod-like) that remain embedded within the CuO tubular matrix (Figure 1e,g,i) can provide additional plasmon-driven photo-excitation pathways. Metallic silver nanostructures are considered as excellent plasmonic materials [68,95,133]. The valence electron clouds present in their metal surfaces can oscillate and resonate at different frequencies in the UV-Vis-NIR ranges generating localized surface plasmons (LSPR). The surface plasmons can interact with the CuO nanotubes via radiative damping mechanisms that imply the reemission and/or trapping of light from the metal to the surrounding semiconductor matrix [95,133]. This approximation would be more likely to occur with the larger Ag domains isolated within the CuO nanotubes (Figure 1e–i) where scattering phenomena would be more plausible (Figure 2c) [95,131]. The photocatalytic response under 940 nm wavelengths can be also tentative attributed in part to the presence of rod-shaped Ag structures entangled within the CuO matrix (Figures 1g and 3b). These anisotropic silver nanostructures exhibit plasmon absorbance at longer wavelengths than spheres or cubes (Figure 1g) [68]. The presence of silver expands the absorption and

light-trapping capabilities in the visible-NIR range, thereby expanding the potential exploitation of the solar energy (more than 80% of the solar spectrum range) [68,92].

Surface plasmons can alternatively decay via non-radiative pathways involving the generation of electron-hole pairs by interband and/or intraband excitations [68,81,92,95]. In this scenario, Ag and CuO entangled interfaces can form a metal/p-type semiconductor Schottky barrier for holes after matching their Fermi levels [3,55,119]. The excitation with sufficiently high energy LEDs (i.e., 405 and 460 nm, Figures 3 and 4b) enables the plasmon-induced injection of hot holes from the silver bands into the valence band of the CuO p-type semiconductor (Figure 4b). These high energetic holes are able to pass the Schottky barrier and rapidly react with the n-hexane. The reduced dimensions of the heteronanostructures minimize the probability of undergoing another relaxation/recombination process [68]. While the injection of hot electrons (using n-type semiconductors such as $TiO_2$) is the most accepted plasmon-driven charge transfer mechanism, there exist recent interesting studies claiming the importance of hot holes in other plasmonic-based systems [73,86,92,97,134–137] such as Au-NiO$_x$, Au-pGaN [73], Au nanorods coated with a CoO nanoshell [138], Au nanostructures [101,139,140], or Ag-BiOCl hybrids [86,137].

We tentatively propose a combination of the different photocatalytic mechanisms given the diversity of Ag domains. Indeed, the better photoresponse of the Ag-CuO hybrid in comparison with the CuO nanostructures confirms the important role of silver as plasmonic structure to harvest light in the whole visible to NIR range. Likewise, the close contact between both metal and semiconductor phases has enabled a suitable interfacial contact to promote electron and holes mobilities and minimize undesired recombination and relaxation pathways. In summary, we can conclude that our Ag-CuO represents a very attractive metal/p-type semiconductor candidate with full-spectrum response that can be envisioned as an affordable alternative for green and sustainable photo-assisted chemistry, with special attention to energy and remediation processes.

## References

1. Kamal, M.S.; Razzak, S.A.; Hossain, M.M. Catalytic oxidation of volatile organic compounds (VOCs)—A review. *Atmos. Environ.* **2016**, *140*, 117–134. [CrossRef]

2. He, C.; Cheng, J.; Zhang, X.; Douthwaite, M.; Pattisson, S.; Hao, Z.P. Recent Advances in the Catalytic Oxidation of Volatile Organic Compounds: A Review Based on Pollutant Sorts and Sources. *Chem. Rev.* **2019**, *119*, 4471–4568. [CrossRef]

3. Huang, H.B.; Xu, Y.; Feng, Q.Y.; Leung, D.Y.C. Low temperature catalytic oxidation of volatile organic compounds: A review. *Catal. Sci. Technol.* **2015**, *5*, 2649–2669. [CrossRef]

4. Smielowska, M.; Marc, M.; Zabiegala, B. Indoor air quality in public utility environments—A review. *Environ. Sci. Pollut. Res.* **2017**, *24*, 11166–11176. [CrossRef] [PubMed]

5. Mamaghani, A.H.; Haghighat, F.; Lee, C.S. Photocatalytic oxidation technology for indoor environment air purification: The state-of-the-art. *Appl. Catal. B Environ.* **2017**, *203*, 247–269. [CrossRef]

6. Kim, H.H.; Teramoto, Y.; Negishi, N.; Ogata, A. A multidisciplinary approach to understand the interactions of nonthermal plasma and catalyst: A review. *Catal. Today* **2015**, *256*, 13–22. [CrossRef]

7. Zhang, Z.X.; Jiang, Z.; Shangguan, W.F. Low-temperature catalysis for VOCs removal in technology and application: A state-of-the-art review. *Catal. Today* **2016**, *264*, 270–278. [CrossRef]

8. Hueso, J.L.; Cotrino, J.; Caballero, A.; Espinos, J.P.; Gonzalez-Elipe, A.R. Plasma catalysis with perovskite-type catalysts for the removal of NO and CH4 from combustion exhausts. *J. Catal.* **2007**, *247*, 288–297. [CrossRef]

9. Mao, L.G.; Chen, Z.Z.; Wu, X.Y.; Tang, X.J.; Yao, S.L.; Zhang, X.M.; Jiang, B.Q.; Han, J.Y.; Wu, Z.L.; Lu, H.; et al. Plasma-catalyst hybrid reactor with $CeO_2$/gamma-$Al_2O_3$ for benzene decomposition with synergetic effect and nano particle by-product reduction. *J. Hazard. Mater.* **2018**, *347*, 150–159. [CrossRef]

10. Nigar, H.; Sturm, G.S.J.; Garcia-Banos, B.; Penaranda-Foix, F.L.; Catala-Civera, J.M.; Mallada, R.; Stankiewicz, A.; Santamaria, J. Numerical analysis of microwave heating cavity: Combining electromagnetic energy, heat transfer and fluid dynamics for a NaY zeolite fixed-bed. *Appl. Therm. Eng.* **2019**, *155*, 226–238. [CrossRef]

11. Nigar, H.; Julian, I.; Mallada, R.; Santamaria, J. Microwave-Assisted Catalytic Combustion for the Efficient Continuous Cleaning of VOC-Containing Air Streams. *Environ. Sci. Technol.* **2018**, *52*, 5892–5901. [CrossRef] [PubMed]

12. Nigar, H.; Navascues, N.; De la Iglesia, O.; Mallada, R.; Santamaria, J. Removal of VOCs at trace concentration levels from humid air by Microwave Swing Adsorption, kinetics and proper sorbent selection. *Sep. Purif. Technol.* **2015**, *151*, 193–200. [CrossRef]

13. Yang, X.G.; Wang, D.W. Photocatalysis: From Fundamental Principles to Materials and Applications. *ACS Appl. Energ. Mater.* **2018**, *1*, 6657–6693. [CrossRef]

14. Kumari, G.; Zhang, X.Q.; Devasia, D.; Heo, J.; Jain, P.K. Watching Visible Light-Driven $CO_2$ Reduction on a Plasmonic Nanoparticle Catalyst. *ACS Nano* **2018**, *12*, 8330–8340. [CrossRef] [PubMed]

15. Brigden, C.T.; Poulston, S.; Twigg, M.V.; Walker, A.P.; Wilkins, A.J.J. Photo-oxidation of short-chain hydrocarbons over titania. *Appl. Catal. B Environ.* **2001**, *32*, 63–71. [CrossRef]

16. Chen, J.Y.; He, Z.G.; Li, G.Y.; An, T.C.; Shi, H.X.; Li, Y.Z. Visible-light-enhanced photothermocatalytic activity of ABO(3)-type perovskites for the decontamination of gaseous styrene. *Appl. Catal. B Environ.* **2017**, *209*, 146–154. [CrossRef]

17. Deng, X.Y.; Yue, Y.H.; Gao, Z. Gas-phase photo-oxidation of organic compounds over nanosized TiO2 photocatalysts by various preparations. *Appl. Catal. B Environ.* **2002**, *39*, 135–147. [CrossRef]

18. Boulamanti, A.K.; Philippopoulos, C.J. Photocatalytic degradation of C-5-C-7 alkanes in the gas-phase. *Atmos. Environ.* **2009**, *43*, 3168–3174. [CrossRef]

19. Boyjoo, Y.; Sun, H.Q.; Liu, J.; Pareek, V.K.; Wang, S.B. A review on photocatalysis for air treatment: From catalyst development to reactor design. *Chem. Eng. J.* **2017**, *310*, 537–559. [CrossRef]

20. Bueno-Alejo, C.J.; Hueso, J.L.; Mallada, R.; Julian, I.; Santamaria, J. High-radiance LED-driven fluidized bed photoreactor for the complete oxidation of n-hexane in air. *Chem. Eng. J.* **2019**, *358*, 1363–1370. [CrossRef]

21. Liotta, L.F.; Ousmane, M.; Di Carlo, G.; Pantaleo, G.; Deganello, G.; Marci, G.; Retailleau, L.; Giroir-Fendler, A. Total oxidation of propene at low temperature over $Co_3O_4$-$CeO_2$ mixed oxides: Role of surface oxygen vacancies and bulk oxygen mobility in the catalytic activity. *Appl. Catal. A Gen.* **2008**, *347*, 81–88. [CrossRef]

22. Ousmane, M.; Liotta, L.F.; Di Carlo, G.; Pantaleo, G.; Venezia, A.M.; Deganello, G.; Retailleau, L.; Boreave, A.; Giroir-Fendler, A. Supported Au catalysts for low-temperature abatement of propene and toluene, as model VOCs: Support effect. *Appl. Catal. B Environ.* **2011**, *101*, 629–637. [CrossRef]

23. Scire, S.; Liotta, L.F. Supported gold catalysts for the total oxidation of volatile organic compounds. *Appl. Catal. B Environ.* **2012**, *125*, 222–246. [CrossRef]

24. Liotta, L.F.; Wu, H.J.; Pantaleo, G.; Venezia, A.M. $Co_3O_4$ nanocrystals and $Co_3O_4$-MOx binary oxides for CO, $CH_4$ and VOC oxidation at low temperatures: A review. *Catal. Sci. Technol.* **2013**, *3*, 3085–3102. [CrossRef]

25. Ousmane, M.; Liotta, L.F.; Pantaleo, G.; Venezia, A.M.; Di Carlo, G.; Aouine, M.; Retailleau, L.; Giroir-Fendler, A. Supported Au catalysts for propene total oxidation: Study of support morphology and gold particle size effects. *Catal. Today* **2011**, *176*, 7–13. [CrossRef]

26. Grabchenko, M.V.; Mikheeva, N.N.; Mamontov, G.V.; Salaev, M.A.; Liotta, L.F.; Vodyankina, O.V. Ag/$CeO_2$ Composites for Catalytic Abatement of CO, Soot and VOCs. *Catalysts* **2018**, *8*, 285. [CrossRef]

27. Sihaib, Z.; Puleo, F.; Pantaleo, G.; La Parola, V.; Valverde, J.L.; Gil, S.; Liotta, L.F.; Giroir-Fendler, A. The Effect of Citric Acid Concentration on the Properties of $LaMnO_3$ as a Catalyst for Hydrocarbon Oxidation. *Catalysts* **2019**, *9*, 226. [CrossRef]

28. Liu, L.C.; Corma, A. Metal Catalysts for Heterogeneous Catalysis: From Single Atoms to Nanoclusters and Nanoparticles. *Chem. Rev.* **2018**, *118*, 4981–5079. [CrossRef]

29. Yang, C.T.; Miao, G.; Pi, Y.H.; Xia, Q.B.; Wu, J.L.; Li, Z.; Xiao, J. Abatement of various types of VOCs by adsorption/catalytic oxidation: A review. *Chem. Eng. J.* **2019**, *370*, 1128–1153. [CrossRef]

30. Uson, L.; Hueso, J.L.; Sebastian, V.; Arenal, R.; Florea, I.; Irusta, S.; Arruebo, M.; Santamaria, J. In-situ preparation of ultra-small Pt nanoparticles within rod-shaped mesoporous silica particles: 3-D tomography and catalytic oxidation of n-hexane. *Catal. Commun.* **2017**, *100*, 93–97. [CrossRef]

31. Uson, L.; Colmenares, M.G.; Hueso, J.L.; Sebastian, V.; Balas, F.; Arruebo, M.; Santamaria, J. VOCs abatement using thick eggshell Pt/SBA-15 pellets with hierarchical porosity. *Catal. Today* **2014**, *227*, 179–186. [CrossRef]

32. Hueso, J.L.; Sebastian, V.; Mayoral, A.; Uson, L.; Arruebo, M.; Santamaria, J. Beyond gold: rediscovering tetrakis-(hydroxymethyl)-phosphonium chloride (THPC) as an effective agent for the synthesis of ultra-small noble metal nanoparticles and Pt-containing nanoalloys. *RSC Adv.* **2013**, *3*, 10427–10433. [CrossRef]

33. Kumar, G.; Nikolla, E.; Linic, S.; Medlin, J.W.; Janik, M.J. Multicomponent Catalysts: Limitations and Prospects. *ACS Catal.* **2018**, *8*, 3202–3208. [CrossRef]

34. Cellier, C.; Lambert, S.; Gaigneaux, E.M.; Poleunis, C.; Ruaux, V.; Eloy, P.; Lahousse, C.; Bertrand, P.; Pirard, J.P.; Grange, P. Investigation of the preparation and activity of gold catalysts in the total oxidation of n-hexane. *Appl. Catal. B Environ.* **2007**, *70*, 406–416. [CrossRef]

35. Liotta, L.F. Catalytic oxidation of volatile organic compounds on supported noble metals. *Appl. Catal. B-Environ.* **2010**, *100*, 403–412. [CrossRef]

36. Guo, J.H.; Lin, C.X.; Jiang, C.J.; Zhang, P.Y. Review on noble metal-based catalysts for formaldehyde oxidation at room temperature. *Appl. Surf. Sci.* **2019**, *475*, 237–255. [CrossRef]

37. Liotta, L.F.; Ousmane, M.; Di Carlo, G.; Pantaleo, G.; Deganello, G.; Boreave, A.; Giroir-Fendler, A. Catalytic Removal of Toluene over $Co_3O_4$-$CeO_2$ Mixed Oxide Catalysts: Comparison with Pt/$Al_2O_3$. *Catal. Lett.* **2009**, *127*, 270–276. [CrossRef]

38. Pereniguez, R.; Hueso, J.L.; Gaillard, F.; Holgado, J.P.; Caballero, A. Study of Oxygen Reactivity in La1-x Sr (x) $CoO_3$-delta Perovskites for Total Oxidation of Toluene. *Catal. Lett.* **2012**, *142*, 408–416. [CrossRef]

39. Pereniguez, R.; Hueso, J.L.; Holgado, J.P.; Gaillard, F.; Caballero, A. Reactivity of LaNi1-y Co (y) $O_3$-delta Perovskite Systems in the Deep Oxidation of Toluene. *Catal. Lett.* **2009**, *131*, 164–169. [CrossRef]

40. Szabo, V.; Bassir, M.; Gallot, J.E.; Van Neste, A.; Kaliaguine, S. Perovskite-type oxides synthesised by reactive grinding–Part III. Kinetics of n-hexane oxidation over LaCo(1-x)FexO3. *Appl. Catal. B Environ.* **2003**, *42*, 265–277. [CrossRef]

41. Rhodes, C.J. Perovskites - some snapshots of recent developments. *Sci. Prog.* **2018**, *101*, 384–396. [CrossRef]

42. Njagi, E.C.; Genuino, H.C.; King'ondu, C.K.; Dharmarathna, S.; Suib, S.L. Catalytic oxidation of ethylene at low temperatures using porous copper manganese oxides. *Appl. Catal. A Gen.* **2012**, *421*, 154–160. [CrossRef]

43. Genuino, H.C.; Dharmarathna, S.; Njagi, E.C.; Mei, M.C.; Suib, S.L. Gas-Phase Total Oxidation of Benzene, Toluene, Ethylbenzene, and Xylenes Using Shape-Selective Manganese Oxide and Copper Manganese Oxide Catalysts. *J. Phys. Chem. C* **2012**, *116*, 12066–12078. [CrossRef]

44. Cordi, E.M.; O'Neill, P.J.; Falconer, J.L. Transient oxidation of volatile organic compounds on a CuO/$Al_2O_3$ catalyst. *Appl. Catal. B-Environ.* **1997**, *14*, 23–36. [CrossRef]

45. Li, T.Y.; Chiang, S.J.; Liaw, B.J.; Chen, Y.Z. Catalytic oxidation of benzene over CuO/Ce1-x$MnxO_2$ catalysts. *Appl. Catal. B Environ.* **2011**, *103*, 143–148. [CrossRef]

46. Liu, B.S.; Wu, H.; Parkin, I.P. Gaseous Photocatalytic Oxidation of Formic Acid over $TiO_2$: A Comparison between the Charge Carrier Transfer and Light-Assisted Mars-van Krevelen Pathways. *J. Phys. Chem. C* **2019**, *123*, 22261–22272. [CrossRef]

47. Shah, K.W.; Li, W.X. A Review on Catalytic Nanomaterials for Volatile Organic Compounds VOC Removal and Their Applications for Healthy Buildings. *Nanomaterials* **2019**, *9*, 910. [CrossRef]

48. Kontos, A.G.; Katsanaki, A.; Maggos, T.; Likodimos, V.; Ghicov, A.; Kim, D.; Kunze, J.; Vasilakos, C.; Schmuki, P.; Falaras, P. Photocatalytic degradation of gas pollutants on self-assembled titania nanotubes. *Chem. Phys. Lett.* **2010**, *490*, 58–62. [CrossRef]

49. Van Gerven, T.; Mul, G.; Moulijn, J.; Stankiewicz, A. A review of intensification of photocatalytic processes. *Chem. Eng. Process.* **2007**, *46*, 781–789. [CrossRef]

50. Da Costa, B.M.; Araujo, A.L.P.; Silva, G.V.; Boaventura, R.A.R.; Dias, M.M.; Lopes, J.C.B.; Vilar, V.J.P. Intensification of heterogeneous TiO$_2$ photocatalysis using an innovative micro-meso-structured-photoreactor for n-decane oxidation at gas phase. *Chem. Eng. J.* **2017**, *310*, 331–341. [CrossRef]

51. Moulis, F.; Krysa, J. Photocatalytic degradation of several VOCs (n-hexane, n-butyl acetate and toluene) on TiO2 layer in a closed-loop reactor. *Catal. Today* **2013**, *209*, 153–158. [CrossRef]

52. Chen, J.; Li, Y.Z.; Fang, S.M.; Yang, Y.; Zhao, X.J. UV-Vis-infrared light-driven thermocatalytic abatement of benzene on Fe doped OMS-2 nanorods enhanced by a novel photoactivation. *Chem. Eng. J.* **2018**, *332*, 205–215. [CrossRef]

53. Wang, L.J.; Zhou, Q.; Zhang, G.L.; Liang, Y.J.; Wang, B.S.; Zhang, W.W.; Lei, B.; Wang, W.Z. A facile room temperature solution-phase route to synthesize CuO nanowires with enhanced photocatalytic performance. *Mater. Lett.* **2012**, *74*, 217–219. [CrossRef]

54. Wu, S.M.; Li, F.; Zhang, L.J.; Li, Z. Enhanced field emission properties of CuO nanoribbons decorated with Ag nanoparticles. *Mater. Lett.* **2016**, *171*, 220–223. [CrossRef]

55. Yang, J.B.; Li, Z.; Zhao, W.; Zhao, C.X.; Wang, Y.; Liu, X.Q. Controllable synthesis of Ag-CuO composite nanosheets with enhanced photocatalytic property. *Mater. Lett.* **2014**, *120*, 16–19. [CrossRef]

56. Yang, Y.; Li, Y.Z.; Zhang, Q.; Zeng, M.; Wu, S.W.; Lan, L.; Zhao, X.J. Novel photoactivation and solar-light-driven thermocatalysis on epsilon-MnO$_2$ nanosheets lead to highly efficient catalytic abatement of ethyl acetate without acetaldehyde as unfavorable by-product. *J. Mater. Chem. A* **2018**, *6*, 14195–14206. [CrossRef]

57. Chang, Y.C.; Guo, J.Y. Double-sided plasmonic silver nanoparticles decorated copper oxide/zinc oxide heterostructured nanomaces with improving photocatalytic performance. *J. Photochem. Photobiol. A Chem.* **2019**, *378*, 184–191. [CrossRef]

58. Zhang, X.D.; Yang, Y.; Li, H.X.; Zou, X.J.; Wang, Y.X. Non-TiO$_2$ Photocatalysts Used for Degradation of Gaseous VOCs. *Prog. Chem.* **2016**, *28*, 1550–1559.

59. Liu, X.Q.; Iocozzia, J.; Wang, Y.; Cui, X.; Chen, Y.H.; Zhao, S.Q.; Li, Z.; Lin, Z.Q. Noble metal-metal oxide nanohybrids with tailored nanostructures for efficient solar energy conversion, photocatalysis and environmental remediation. *Energy Environ. Sci.* **2017**, *10*, 402–434. [CrossRef]

60. Almquist, C.B.; Biswas, P. The photo-oxidation of cyclohexane on titanium dioxide: An investigation of competitive adsorption and its effects on product formation and selectivity. *Appl. Catal. A Gen.* **2001**, *214*, 259–271. [CrossRef]

61. Tsoncheva, T.; Issa, G.; Blasco, T.; Dimitrov, M.; Popova, M.; Hernandez, S.; Kovacheva, D.; Atanasova, G.; Nieto, J.M.L. Catalytic VOCs elimination over copper and cerium oxide modified mesoporous SBA-15 silica. *Appl. Catal. A Gen.* **2013**, *453*, 1–12. [CrossRef]

62. Carrillo, A.M.; Carriazo, J.G. Cu and Co oxides supported on halloysite for the total oxidation of toluene. *Appl. Catal. B Environ.* **2015**, *164*, 443–452. [CrossRef]

63. Cui, E.T.; Hou, G.H.; Chen, X.H.; Zhang, F.; Deng, Y.X.; Yu, G.Y.; Li, B.B.; Wu, Y.Q. In-situ hydrothermal fabrication of Sr$_2$FeTaO$_6$/NaTaO$_3$ heterojunction photocatalyst aimed at the effective promotion of electron-hole separation and visible-light absorption. *Appl. Catal. B Environ.* **2019**, *241*, 52–65. [CrossRef]

64. Li, J.J.; Yu, E.Q.; Cai, S.C.; Chen, X.; Chen, J.; Jia, H.P.; Xu, Y.J. Noble metal free, CeO$_2$/LaMnO$_3$ hybrid achieving efficient photo-thermal catalytic decomposition of volatile organic compounds under IR light. *Appl. Catal. B Environ.* **2019**, *240*, 141–152. [CrossRef]

65. Liu, Y.; Zhang, Z.Y.; Fang, Y.R.; Liu, B.K.; Huang, J.D.; Miao, F.J.; Bao, Y.A.; Dong, B. IR-Driven strong plasmonic-coupling on Ag nanorices/W$_{18}$O$_{49}$ nanowires heterostructures for photo/thermal synergistic enhancement of H-2 evolution from ammonia borane. *Appl. Catal. B Environ.* **2019**, *252*, 164–173. [CrossRef]

66. Lee, Y.E.; Chung, W.C.; Chang, M.B. Photocatalytic oxidation of toluene and isopropanol by LaFeO$_3$/black-TiO$_2$. *Environ. Sci. Pollut. Res.* **2019**, *26*, 20908–20919. [CrossRef]

67. Ray, C.; Pal, T. Recent advances of metal-metal oxide nanocomposites and their tailored nanostructures in numerous catalytic applications. *J. Mater. Chem. A* **2017**, *5*, 9465–9487. [CrossRef]

68. Valenti, M.; Jonsson, M.P.; Biskos, G.; Schmidt-Ott, A.; Smith, W.A. Plasmonic nanoparticle-semiconductor composites for efficient solar water splitting. *J. Mater. Chem. A* **2016**, *4*, 17891–17912. [CrossRef]

69. Wu, N.Q. Plasmonic metal-semiconductor photocatalysts and photoelectrochemical cells: A review. *Nanoscale* **2018**, *10*, 2679–2696. [CrossRef]

70. Mendez-Medrano, M.G.; Kowalska, E.; Lehoux, A.; Herissan, A.; Ohtani, B.; Bahena, D.; Briois, V.; Colbeau-Justin, C.; Rodriguez-Lopez, J.L.; Remita, H. Surface Modification of $TiO_2$ with Ag Nanoparticles and CuO Nanoclusters for Application in Photocatalysis. *J. Phys. Chem. C* **2016**, *120*, 5143–5154. [CrossRef]

71. Boriskina, S.V.; Ghasemi, H.; Chen, G. Plasmonic materials for energy: From physics to applications. *Mater. Today* **2013**, *16*, 375–386. [CrossRef]

72. Zhang, X.D.; Yang, Y.; Song, L.; Wang, Y.X.; He, C.; Wang, Z.; Cui, L.F. High and stable catalytic activity of $Ag/Fe_2O_3$ catalysts derived from MOFs for CO oxidation. *Mol. Catal.* **2018**, *447*, 80–89. [CrossRef]

73. DuChene, J.S.; Tagliabue, G.; Welch, A.J.; Cheng, W.H.; Atwater, H.A. Hot Hole Collection and Photoelectrochemical $CO_2$ Reduction with Plasmonic Au/p-GaN Photocathodes. *Nano Lett.* **2018**, *18*, 2545–2550. [CrossRef] [PubMed]

74. Kim, Y.; Torres, D.D.; Jain, P.K. Activation Energies of Plasmonic Catalysts. *Nano Lett.* **2016**, *16*, 3399–3407. [CrossRef]

75. Khiavi, N.D.; Katal, R.; Eshkalak, S.K.; Masudy-Panah, S.; Ramakrishna, S.; Hu, J.Y. Visible Light Driven Heterojunction Photocatalyst of $CuO-Cu_2O$ Thin Films for Photocatalytic Degradation of Organic Pollutants. *Nanomaterials* **2019**, *9*, 1011. [CrossRef]

76. Christopher, P.; Xin, H.L.; Linic, S. Visible-light-enhanced catalytic oxidation reactions on plasmonic silver nanostructures. *Nat. Chem.* **2011**, *3*, 467–472. [CrossRef]

77. Leong, K.H.; Abd Aziz, A.; Sim, L.C.; Saravanan, P.; Jang, M.; Bahnemann, D. Mechanistic insights into plasmonic photocatalysts in utilizing visible light. *Beilstein J. Nanotechnol.* **2018**, *9*, 628–648. [CrossRef]

78. Ma, L.; Chen, S.; Shao, Y.; Chen, Y.L.; Liu, M.X.; Li, H.X.; Mao, Y.L.; Ding, S.J. Recent Progress in Constructing Plasmonic Metal/Semiconductor Hetero-Nanostructures for Improved Photocatalysis. *Catalysts* **2018**, *8*, 634. [CrossRef]

79. Truppi, A.; Petronella, F.; Placido, T.; Striccoli, M.; Agostiano, A.; Curri, M.L.; Comparelli, R. Visible-Light-Active $TiO_2$-Based Hybrid Nanocatalysts for Environmental Applications. *Catalysts* **2017**, *7*, 100. [CrossRef]

80. Zhang, Y.C.; He, S.; Guo, W.X.; Hu, Y.; Huang, J.W.; Mulcahy, J.R.; Wei, W.D. Surface-Plasmon-Driven Hot Electron Photochemistry. *Chem. Rev.* **2018**, *118*, 2927–2954. [CrossRef]

81. Tatsuma, T.; Nishi, H.; Ishida, T. Plasmon-induced charge separation: chemistry and wide applications. *Chem. Sci.* **2017**, *8*, 3325–3337. [CrossRef] [PubMed]

82. Erwin, W.R.; Zarick, H.F.; Talbert, E.M.; Bardhan, R. Light trapping in mesoporous solar cells with plasmonic nanostructures. *Energy Environ. Sci.* **2016**, *9*, 1577–1601. [CrossRef]

83. Araujo, T.P.; Quiroz, J.; Barbosa, E.C.M.; Camargo, P.H.C. Understanding plasmonic catalysis with controlled nanomaterials based on catalytic and plasmonic metals. *Curr. Opin. Colloid Interface Sci.* **2019**, *39*, 110–122. [CrossRef]

84. Mao, M.Y.; Li, Y.Z.; Lv, H.Q.; Hou, J.T.; Zeng, M.; Ren, L.; Huang, H.; Zhao, X.J. Efficient UV-vis-IR light-driven thermocatalytic purification of benzene on a $Pt/CeO_2$ nanocomposite significantly promoted by hot electron-induced photoactivation. *Environ. Sci. Nano* **2017**, *4*, 373–384. [CrossRef]

85. Fu, S.F.; Zheng, Y.; Zhou, X.B.; Ni, Z.M.; Xia, S.J. Visible light promoted degradation of gaseous volatile organic compounds catalyzed by Au supported layered double hydroxides: Influencing factors, kinetics and mechanism. *J. Hazard. Mater.* **2019**, *363*, 41–54. [CrossRef]

86. Ma, X.C.; Dai, Y.; Yu, L.; Huang, B.B. Energy transfer in plasmonic photocatalytic composites. *Light Sci. Appl.* **2016**, *5*, e16017. [CrossRef]

87. Gomez, L.; Hueso, J.L.; Ortega-Liebana, M.C.; Santamaria, J.; Cronin, S.B. Evaluation of gold-decorated halloysite nanotubes as plasmonic photocatalysts. *Catal. Commun.* **2014**, *56*, 115–118. [CrossRef]

88. Graus, J.; Bueno-Alejo, C.J.; Hueso, J.L. In-Situ Deposition of Plasmonic Gold Nanotriangles and Nanoprisms onto Layered Hydroxides for Full-Range Photocatalytic Response towards the Selective Reduction of p-Nitrophenol. *Catalysts* **2018**, *8*, 354. [CrossRef]

89. Uson, L.; Sebastian, V.; Mayoral, A.; Hueso, J.L.; Eguizabal, A.; Arruebo, M.; Santamaria, J. Spontaneous formation of Au-Pt alloyed nanoparticles using pure nano-counterparts as starters: A ligand and size dependent process. *Nanoscale* **2015**, *7*, 10152–10161. [CrossRef]

90. Zieba, M.; Hueso, J.L.; Arruebo, M.; Martinez, G.; Santamaria, J. Gold-coated halloysite nanotubes as tunable plasmonic platforms. *New J. Chem.* **2014**, *38*, 2037–2042. [CrossRef]

91. Halas, N.J.; Lal, S.; Chang, W.S.; Link, S.; Nordlander, P. Plasmons in Strongly Coupled Metallic Nanostructures. *Chem. Rev.* **2011**, *111*, 3913–3961. [CrossRef] [PubMed]

92. Aslam, U.; Rao, V.G.; Chavez, S.; Linic, S. Catalytic conversion of solar to chemical energy on plasmonic metal nanostructures. *Nat. Catal.* **2018**, *1*, 656–665. [CrossRef]

93. Kim, Y.; Smith, J.G.; Jain, P.K. Harvesting multiple electron-hole pairs generated through plasmonic excitation of Au nanoparticles. *Nat. Chem.* **2018**, *10*, 763–769. [CrossRef] [PubMed]

94. Bernardi, M.; Mustafa, J.; Neaton, J.B.; Louie, S.G. Theory and computation of hot carriers generated by surface plasmon polaritons in noble metals. *Nat. Commun.* **2015**, *6*, 7044. [CrossRef] [PubMed]

95. Brongersma, M.L.; Halas, N.J.; Nordlander, P. Plasmon-induced hot carrier science and technology. *Nat. Nanotechnol.* **2015**, *10*, 25–34. [CrossRef]

96. Kriegel, I.; Scotognella, F.; Manna, L. Plasmonic doped semiconductor nanocrystals: Properties, fabrication, applications and perspectives. *Phys. Rep. Rev. Sec. Phys. Lett.* **2017**, *674*, 1–52. [CrossRef]

97. Rao, V.G.; Aslam, U.; Linic, S. Chemical Requirement for Extracting Energetic Charge Carriers from Plasmonic Metal Nanoparticles to Perform Electron-Transfer Reactions. *J. Am. Chem. Soc.* **2019**, *141*, 643–647. [CrossRef]

98. Aslam, U.; Chavez, S.; Linic, S. Controlling energy flow in multimetallic nanostructures for plasmonic catalysis. *Nat. Nanotechnol.* **2017**, *12*, 1000–1005. [CrossRef]

99. Boerigter, C.; Aslam, U.; Linic, S. Mechanism of Charge Transfer from Plasmonic Nanostructures to Chemically Attached Materials. *ACS Nano* **2016**, *10*, 6108–6115. [CrossRef]

100. Linic, S.; Aslam, U.; Boerigter, C.; Morabito, M. Photochemical transformations on plasmonic metal nanoparticles. *Nat. Mater.* **2015**, *14*, 567–576. [CrossRef]

101. Gargiulo, J.; Berte, R.; Li, Y.; Maier, S.A.; Cortes, E. From Optical to Chemical Hot Spots in Plasmonics. *Acc. Chem. Res.* **2019**, *52*, 2525–2535. [CrossRef]

102. Linic, S.; Christopher, P.; Xin, H.L.; Marimuthu, A. Catalytic and Photocatalytic Transformations on Metal Nanoparticles with Targeted Geometric and Plasmonic Properties. *Acc. Chem. Res.* **2013**, *46*, 1890–1899. [CrossRef]

103. Brus, L. Noble Metal Nanocrystals: Plasmon Electron Transfer Photochemistry and Single-Molecule Raman Spectroscopy. *Acc. Chem. Res.* **2008**, *41*, 1742–1749. [CrossRef]

104. El-Sayed, M.A. Some interesting properties of metals confined in time and nanometer space of different shapes. *Acc. Chem. Res.* **2001**, *34*, 257–264. [CrossRef]

105. Marimuthu, A.; Zhang, J.W.; Linic, S. Tuning Selectivity in Propylene Epoxidation by Plasmon Mediated Photo-Switching of Cu Oxidation State. *Science* **2013**, *339*, 1590–1593. [CrossRef]

106. Wan, L.L.; Zhou, Q.X.; Wang, X.; Wood, T.E.; Wang, L.; Duchesne, P.N.; Guo, J.L.; Yan, X.L.; Xia, M.K.; Lie, Y.F.; et al. $Cu_2O$ nanocubes with mixed oxidation-state facets for (photo)catalytic hydrogenation of carbon dioxide. *Nat. Catal.* **2019**, *2*, 889–898. [CrossRef]

107. Zhang, Q.B.; Zhang, K.L.; Xu, D.G.; Yang, G.C.; Huang, H.; Nie, F.D.; Liu, C.M.; Yang, S.H. CuO nanostructures: Synthesis, characterization, growth mechanisms, fundamental properties, and applications. *Prog. Mater. Sci.* **2014**, *60*, 208–337. [CrossRef]

108. Kumar, M.K.; Bhavani, K.; Naresh, G.; Srinivas, B.; Venugopal, A. Plasmonic resonance nature of Ag-Cu/TiO$_2$ photocatalyst under solar and artificial light: Synthesis, characterization and evaluation of H$_2$O splitting activity. *Appl. Catal. B Environ.* **2016**, *199*, 282–291.

109. Nguyen, N.L.; de Gironcoli, S.; Piccinin, S. Ag-Cu catalysts for ethylene epoxidation: Selectivity and activity descriptors. *J. Chem. Phys.* **2013**, *138*, 184707. [CrossRef]

110. Rapallo, A.; Rossi, G.; Ferrando, R.; Fortunelli, A.; Curley, B.C.; Lloyd, L.D.; Tarbuck, G.M.; Johnston, R.L. Global optimization of bimetallic cluster structures. I. Size-mismatched Ag-Cu, Ag-Ni, and Au-Cu systems. *J. Chem. Phys.* **2005**, *122*, 194308. [CrossRef]

111. Verma, A.; Gupta, R.K.; Shukla, M.; Malviya, M.; Sinha, I. Ag-Cu Bimetallic Nanoparticles as Efficient Oxygen Reduction Reaction Electrocatalysts in Alkaline Media. *J. Nanosci. Nanotechnol.* **2020**, *20*, 1765–1772. [CrossRef] [PubMed]

112. Piccinin, S.; Zafeiratos, S.; Stampfl, C.; Hansen, T.W.; Havecker, M.; Teschner, D.; Bukhtiyarov, V.I.; Girgsdies, F.; Knop-Gericke, A.; Schlogl, R.; et al. Alloy Catalyst in a Reactive Environment: The Example of Ag-Cu Particles for Ethylene Epoxidation. *Phys. Rev. Lett.* **2010**, *104*, 035503. [CrossRef] [PubMed]

113. Tchaplyguine, M.; Zhang, C.F.; Andersson, T.; Bjorneholm, O. Ag-Cu oxide nanoparticles with high oxidation states: towards new high T-c materials. *Dalton Trans.* **2018**, *47*, 16660–16667. [CrossRef] [PubMed]

114. Zhang, Y.Y.; Wang, L.L.; Kong, X.Y.; Jiang, H.Y.; Zhang, F.; Shi, J.S. Novel Ag-Cu bimetallic alloy decorated near-infrared responsive three-dimensional rod-like architectures for efficient photocatalytic water purification. *J. Colloid Interface Sci.* **2018**, *522*, 29–39. [CrossRef] [PubMed]

115. Walsh, D.; Arcelli, L.; Ikoma, T.; Tanaka, J.; Mann, S. Dextran templating for the synthesis of metallic and metal oxide sponges. *Nat. Mater.* **2003**, *2*, 386. [CrossRef] [PubMed]

116. Liang, Y.; Chen, Z.; Yao, W.; Wang, P.Y.; Yu, S.J.; Wang, X.K. Decorating of Ag and CuO on Cu Nanoparticles for Enhanced High Catalytic Activity to the Degradation of Organic Pollutants. *Langmuir* **2017**, *33*, 7606–7614. [CrossRef]

117. Elemike, E.E.; Onwudiwe, D.C.; Ogeleka, D.F.; Mbonu, J.I. Phyto-assisted Preparation of Ag and Ag-CuO Nanoparticles Using Aqueous Extracts of Mimosa pigra and their Catalytic Activities in the Degradation of Some Common Pollutants. *J. Inorg. Organomet. Polym. Mater.* **2019**, *29*, 1798–1806. [CrossRef]

118. Ji, W.K.; Shen, T.; Kong, J.J.; Rui, Z.B.; Tong, Y.X. Synergistic Performance between Visible-Light Photocatalysis and Thermocatalysis for VOCs Oxidation over Robust Ag/F-Codoped SrTiO$_3$. *Ind. Eng. Chem. Res.* **2018**, *57*, 12766–12773. [CrossRef]

119. Wan, X.; Yang, J.; Huang, X.Y.; Tie, S.L.; Lan, S. A high-performance room temperature thermocatalyst Cu$_2$O/Ag-0@Ag-NPs for dye degradation under dark condition. *J. Alloys Compd.* **2019**, *785*, 398–409. [CrossRef]

120. Kung, M.L.; Tai, M.H.; Lin, P.Y.; Wu, D.C.; Wu, W.J.; Yeh, B.W.; Hung, H.S.; Kuo, C.H.; Chen, Y.W.; Hsieh, S.L.; et al. Silver decorated copper oxide (Ag@CuO) nanocomposite enhances ROS-mediated bacterial architecture collapse. *Colloid Surf. B Biointerfaces* **2017**, *155*, 399–407. [CrossRef]

121. Ramirez, A.; Hueso, J.L.; Suarez, H.; Mallada, R.; Ibarra, A.; Irusta, S.; Santamaria, J. A Nanoarchitecture Based on Silver and Copper Oxide with an Exceptional Response in the Chlorine-Promoted Epoxidation of Ethylene. *Angew. Chem. Int. Edit.* **2016**, *55*, 11158–11161. [CrossRef] [PubMed]

122. Bottega-Pergher, B.; Graus, J.; Bueno-Alejo, C.J.; Hueso, J.L. Triangular and Prism-Shaped Gold-Zinc Oxide Plasmonic Nanostructures: In situ Reduction, Assembly, and Full-Range Photocatalytic Performance. *Eur. J. Inorg. Chem.* **2019**, *2019*, 3228–3234. [CrossRef]

123. Ramirez, A.; Hueso, J.L.; Mallada, R.; Santamaria, J. Ethylene epoxidation in microwave heated structured reactors. *Catal. Today* **2016**, *273*, 99–105. [CrossRef]

124. Ramirez, A.; Hueso, J.L.; Mallada, R.; Santamaria, J. In situ temperature measurements in microwave-heated gas-solid catalytic systems. Detection of hot spots and solid-fluid temperature gradients in the ethylene epoxidation reaction. *Chem. Eng. J.* **2017**, *316*, 50–60. [CrossRef]

125. Gomez-Romero, P.; Tejada-Rosales, E.M.; Palacin, M.R. Ag$_2$Cu$_2$O$_3$: The first silver copper oxide. *Angew. Chem. Int. Edit.* **1999**, *38*, 524–525. [CrossRef]

126. Tejada-Rosales, E.M.; Rodriguez-Carvajal, J.; Casan-Pastor, N.; Alemany, P.; Ruiz, E.; El-Fallah, M.S.; Alvarez, S.; Gomez-Romero, P. Room-temperature synthesis and crystal, magnetic, and electronic structure of the first silver copper oxide. *Inorg. Chem.* **2002**, *41*, 6604–6613. [CrossRef]

127. Carreras, A.; Conejeros, S.; Camon, A.; Garcia, A.; Casan-Pastor, N.; Alemany, P.; Canadell, E. Charge Delocalization, Oxidation States, and Silver Mobility in the Mixed Silver-Copper Oxide AgCuO$_2$. *Inorg. Chem.* **2019**, *58*, 7026–7035. [CrossRef]

128. Navaladian, S.; Viswanathan, B.; Viswanath, R.P.; Varadarajan, T.K. Thermal decomposition as route for silver nanoparticles. *Nanoscale Res. Lett.* **2007**, *2*, 44–48. [CrossRef]

129. Boerigter, C.; Campana, R.; Morabito, M.; Linic, S. Evidence and implications of direct charge excitation as the dominant mechanism in plasmon-mediated photocatalysis. *Nat. Commun.* **2016**, *7*, 10545. [CrossRef]

130. Zhang, T.; Wang, S.J.; Zhang, X.Y.; Su, D.; Yang, Y.; Wu, J.Y.; Xu, Y.Y.; Zhao, N. Progress in the Utilization Efficiency Improvement of Hot Carriers in Plasmon-Mediated Heterostructure Photocatalysis. *Appl. Sci.* **2019**, *9*, 2093. [CrossRef]

131. Zhou, L.A.; Swearer, D.F.; Zhang, C.; Robatjazi, H.; Zhao, H.Q.; Henderson, L.; Dong, L.L.; Christopher, P.; Carter, E.A.; Nordlander, P.; et al. Quantifying hot carrier and thermal contributions in plasmonic photocatalysis. *Science* **2018**, *362*, 69–72. [CrossRef] [PubMed]

132. Huang, Y.F.; Zhang, M.; Zhao, L.B.; Feng, J.M.; Wu, D.Y.; Ren, B.; Tian, Z.Q. Activation of Oxygen on Gold and Silver Nanoparticles Assisted by Surface Plasmon Resonances. *Angew. Chem. Int. Edit.* **2014**, *53*, 2353–2357. [CrossRef] [PubMed]

133. Kim, M.; Lee, J.H.; Nam, J.M. Plasmonic Photothermal Nanoparticles for Biomedical Applications. *Adv. Sci.* **2019**, *6*, 1900471. [CrossRef] [PubMed]

134. Brown, A.M.; Sundararaman, R.; Narang, P.; Goddard, W.A.; Atwater, H.A. Nonradiative Plasmon Decay and Hot Carrier Dynamics: Effects of Phonons, Surfaces, and Geometry. *ACS Nano* **2016**, *10*, 957–966. [CrossRef] [PubMed]

135. Atwater, H.A.; Polman, A. Plasmonics for improved photovoltaic devices. *Nat. Mater.* **2010**, *9*, 205–213. [CrossRef] [PubMed]

136. Jermyn, A.S.; Tagliabue, G.; Atwater, H.A.; Goddard, W.A.; Narang, P.; Sundararaman, R. Transport of hot carriers in plasmonic nanostructures. *Phys. Rev. Mater.* **2019**, *3*, 075201. [CrossRef]

137. Bai, S.; Li, X.Y.; Kong, Q.; Long, R.; Wang, C.M.; Jiang, J.; Xiong, Y.J. Toward Enhanced Photocatalytic Oxygen Evolution: Synergetic Utilization of Plasmonic Effect and Schottky Junction via Interfacing Facet Selection. *Adv. Mater.* **2015**, *27*, 3444–3452. [CrossRef]

138. Ghosh, P.; Kar, A.; Khandelwal, S.; Vyas, D.; Mir, A.; Chakraborty, A.L.; Hegde, R.S.; Sharma, S.; Dutta, A.; Khatua, S. Plasmonic CoO-Decorated Au Nanorods for Photoelectrocatalytic Water Oxidation. *ACS Appl. Nano Mater.* **2019**, *2*, 5795–5803. [CrossRef]

139. Al-Zubeidi, A.; Hoener, B.S.; Collins, S.S.E.; Wang, W.X.; Kirchner, S.R.; Jebeli, S.A.H.; Joplin, A.; Chang, W.S.; Link, S.; Landes, C.F. Hot Holes Assist Plasmonic Nanoelectrode Dissolution. *Nano Lett.* **2019**, *19*, 1301–1306. [CrossRef]

140. Pensa, E.; Gargiulo, J.; Lauri, A.; Schlucker, S.; Cortes, E.; Maier, S.A. Spectral Screening of the Energy of Hot Holes over a Particle Plasmon Resonance. *Nano Lett.* **2019**, *19*, 1867–1874. [CrossRef]